1 # Supplementary Information

2 **Interface engineering of porous Co(OH)$_2$/La(OH)$_3$@Cu nanowires**

3 **heterostructure for high efficiency hydrogen evolution and overall water splitting**

4

5 *Zhen Zhang[1], Zhiqiang Wang[2], Hang Zhang[1], Zikuan Zhang[1], Jingwei Zhou[1], Ying*

6 *Hou[1], Peizhi Liu[1], Bingshe Xu[1], Haixia Zhang[1]*, Junjie Guo[1]**

7

8 [1]Key Laboratory of Interface Science and Engineering in Advanced Materials, Ministry

9 of Education, Taiyuan University of Technology, Taiyuan 030024, P. R. China

10 E-mail address: zhanghaixia@tyut.edu.cn; guojunjie@tyut.edu.cn

11

12 [2]Key Laboratory for Advanced Materials and Joint International Research Laboratory

13 for Precision Chemistry and Molecular Engineering, East China University of Science

14 and Technology, Shanghai, 200237, China.

15

16

17

18

19

20

21

1 Experimental sections

2 *Chemicals and materials*

3   Ammonium persulphate ($(NH_4)_2S_2O_8$, AR) and sodium hydroxide (NaOH, AR) were

4   purchased from Macklin Ltd (Shanghai, China). Lanthanum nitrate hexahydrate

5   ($La(NO_3)_3 \cdot 6H_2O$, 99.99%) and Cobalt nitrate hexahydrate ($Co(NO_3)_2 \cdot 6H_2O$, 99.99%)

6   were purchased from Aladdin Chemical Ltd (Shanghai, China). Hydrochloric acid

7   (HCl, AR.) and ethanol (C_2H_5OH, AR.) were purchased from Tianjin Chemical Work.

8   Potassium hydroxide (KOH, AR) was purchased from Sinopharm Chemical Reagent

9   (Shanghai). Ruthenium oxide (RuO_2, 99.9 wt.%) was purchased from Alfa. Nafion (5

10 wt.%, DuPont) was purchased from commercial suppliers. All the materials were

11 utilized in the absence of further purification in this study. The deionized (DI) water

12 employed in the whole experiments was prepared by an ultrapure purification system.

13 *Preparation of CuO NWs*

14 Weighing 1.426 g of $(NH_4)_2S_2O_8$ and 5.000 g of NaOH in a beaker with 50 mL of DI

15 water were stirred until all chemicals dissolved. A piece of copper foam (CF) with a

16 size of 1×3 cm was washed successively in ethanol, 3 M hydrochloric acid and

17 deionized water. Subsequently, the cleaned CF was immersed into above-mentioned

18 solution for 15 min, the $Cu(OH)_2$ NWs on the surface of CF were performed, which

19 were cleaned by DI water and dried at 60 °C. Finally, the $Cu(OH)_2$ NWs were annealed

20 at 180 °C in air for 2 h to obtain the CuO NWs on CF (mark as CuO NWs).

21 *Preparation of CH/LH@Cu NWs*

22 CH/LH was grown onto the surface of CuO NWs by electrodeposition (ED) at 25 °C.

23 The reaction was operated in a three-electrode configuration, where the CuO NWs

loaded on CF (1×1.5 cm) was directly used as the working electrode, Pt foil and saturated calomel electrode (SCE) were used as the counter electrode and the reference electrode, respectively. 7.5 mmol $Co(NO_3)_2 \cdot 6H_2O$ and 6 mmol $La(NO_3)_3 \cdot 6H_2O$ were dissolved in 50 ml DI water as ED electrolyte. The ED was performed by applying a constant potential of −1.0 V vs SCE for 1500 s to obtain $CH/LH@CuO_x$ NWs. Subsequently, a constant potential (−88 mV vs. RHE) was applied to the $CH/LH@CuO_x$ NWs in 1 M KOH for 900 s, when the cathodic current achieved zero at 0 V vs. RHE, CH/LH@Cu NWs was prepared successfully. The products were washed with DI water, then put on filter paper and dried at room temperature. In particular, the porous structure of $Co(OH)_2/La(OH)_3$ could be attributed to the formation of tiny bubbles of H_2 on the working electrode surface during ED.

Preparation of CH/LH

Similar to $CH/LH@CuO_x$ NWs, the CH/LH was synthesized via the same electrodeposition condition except the substrate was CF instead of CuO NWs.

Preparation of Pt/@Cu NWs and RuO$_2$@Cu NWs

Commercial Pt/C or RuO_2 powder was ultrasonically dispersed in a mixture of 500 µL DI water, 500 µL ethanol and 80 µL of 5 wt.% Nafion solution, which was sonicated for 30 min. The formed homogeneous ink was then dropped onto the CuO NWs and dried in air at 25 °C. The mass loading of the Pt/C (or RuO_2) was identical to CH/LH@Cu NWs. A constant potential (−88 mV vs. RHE) was applied to Pt/C@Cu NWs and RuO_2@Cu NWs in 1 M KOH for 900 s, when the cathodic current achieved zero at 0 V vs. RHE, the Pt/C@Cu NWs and RuO_2@Cu NWs samples prepared successfully.

1 *Preparation of Co(OH)$_2$@Cu NWs, La(OH)$_3$@Cu NWs, CH/LH@CuO$_x$ NWs-1,*

2 *CH/LH@CuO$_x$ NWs-2 and CH/LH@CuO$_x$ NWs-3*

3　　Similar to CH/LH@CuO$_x$ NWs, the control samples were also synthesized via the

4 same electrodeposition mode. The electrodeposition potential was −1.0 V vs SCE, and

5 the duration was 300 s. By changing the concentration of Co(NO$_3$)$_2$·6H$_2$O and

6 La(NO$_3$)$_3$·6H$_2$O in ED electrolyte (50 mL) to obtain Co(OH)$_2$@Cu NWs (7.5 mmol

7 Co(NO$_3$)$_2$·6H$_2$O), La(OH)$_3$@Cu NWs (6 mmol La(NO$_3$)$_3$·6H$_2$O), CH/LH@Cu NWs-1

8 (7.5 mmol Co(NO$_3$)$_2$·6H$_2$O and 1.5 mmol La(NO$_3$)$_3$·6H$_2$O), CH/LH@Cu NWs-2 (7.5

9 mmol Co(NO$_3$)$_2$·6H$_2$O and 6 mmol La(NO$_3$)$_3$·6H$_2$O) and CH/LH@Cu NWs-3 (7.5

10 mmol Co(NO$_3$)$_2$·6H$_2$O and 12 mmol La(NO$_3$)$_3$·6H$_2$O).

11 *Materials Characterization*

12　　X-ray diffraction (XRD) patterns were collected on a Bruker D8 (Cu Kα radiation).

13 To eliminate extremely strong Cu diffraction peaks, CH/LH was electrodeposited on

14 CF under the same conditions, and then CH/LH was scraped off from the substrate for

15 XRD analysis. Morphology and structure of the materials were characterized using a

16 scanning electron microscopy (SEM, TESCAN, LYRA3) and a high-resolution

17 transmission electron microscopy (HRTEM, JEOL, JEM-2010F). The energy

18 dispersive X-ray (EDX) was collected using Oxford instruments equipped on SEM and

19 TEM. X-ray photoelectron spectroscopy (XPS) measurements were performed using

20 an Amicus from 10 kV Mg Kα radiation at the pressure of 1×10^{-7} Par. The BET

21 isotherms were evaluated using a nitrogen adsorption-desorption apparatus

22 (Quadrasorb SI, Quantachrome). The chemical elements of the prepared samples were

23 measured by inductively coupled plasma mass spectrometry (ICP-MS, PerkinElmer,

24 Nexion 2000).

1 *Calculation Methods*

2   In this work, all spin-polarized DFT calculations were carried out using the Vienna

3 Ab–initio Simulation Package (VASP).[1] The projector augmented wave (PAW)

4 method[2] and the Perdew-Burke-Ernzerhof (PBE)[3] functional under the generalized

5 gradient approximation (GGA)[4] were applied throughout the calculations. The kinetic

6 energy cut-off was set to 400 eV, and the force threshold in structure optimization was

7 0.05 eV Å^{-1}. We used a large vacuum gap of 15 Å to eliminate the interactions between

8 neighboring slabs.

9   For the model construction, we first built a *p* (3×3) surface slab containing three layers

10 for $Co(OH)_2$ (001) surface, and the top two layers of $Co(OH)_2$ (001) were allowed to

11 fully relax, while the bottom atom layer was kept fixed to mimic the bulk region. Then,

12 we built a *p* (2×3) surface slab containing three layers for $La(OH)_3$ (100) surface, and

13 the top three layers of the $La(OH)_3$(100) were allowed to relax, while the bottom atom

14 layer was kept fixed to mimic the bulk region. Finally, we also built heterojunction

15 CH/LH system, this system main exposed $Co(OH)_2$ (001) surface which was modeled

16 by a *p* (4×4) surface slab (a = b = 12.57 Å, c = 18.98 Å), containing one O−Co−O layer,

17 a *p* (2×2) $La(OH)_3$ (001) surface (a = b = 13.06 Å, c = 16.93 Å), and all atoms were

18 allowed to fully relax. A 2×2×1 *k*-point mesh was used in calculations of all these

19 models. The on-site Coulomb interaction correction was necessary for the appropriate

20 description of the Co 3*d* electrons, and all calculations were performed with U = 3.52

21 eV, which were consistent with the values determined by previous studies.[5]

22   The hydrogen absorption energies (E_{ads}(H)) on different surfaces were calculated as

23     $E_{ads}(H) = E_{(M+H^*)} - E_M - 1/2E_{H2}$

where $E_{(M+H^*)}$ is the total energy of the adsorption system; E_M is calculated energies of the clean surface; E_{H2} is the energy of a hydrogen molecule in the gas phase. The Gibbs free energy for the hydrogen absorption was corrected with entropy and zero point energy as

$$\Delta G_H = E_{ads}(H) + \Delta E_{ZPE} - T \times \Delta S_H$$

where $E_{ads}(H)$ is the hydrogen absorption energy, ΔE_{ZPE} is the difference in zero point energy between the adsorbed hydrogen and hydrogen in the gas phase and ΔS_H is the entropy difference between the adsorbed state and the gas phase, and T is the temperature. The values used for corrections of ΔE_{ZPE} and ΔS were calculated by frequencies and listed in **Table S1**.

Electrocatalytic Measurements

Electrochemical measurements were carried out on a CHI 760E electrochemical workstation (CH Instruments, Inc., Shanghai) in a standard three-electrode system at 25 °C with an aqueous solution of 1.0 M KOH used as the electrolyte. A Hg/HgO (1.0 M KOH) electrode and a graphite rod were used as the reference electrode and counter electrode, respectively. The measured potentials vs Hg/HgO were converted to reversible hydrogen electrode (RHE) according to the equation E(RHE) = E(Hg/HgO) + 0.098 + 0.059 pH. All of the collected linear sweeping voltammetry (LSV) curves were corrected via 95% iR auto-compensation. The polarization curves obtained from LSV measurements were recorded at a scan rate of 5 mV s⁻¹. The long-term durability test was performed using chronopotentiometric measurements. The ECSA was determined by the electrochemical C_{dl} from the scan-rate dependence of cyclic voltammetry (CV). All Electrochemical impedance spectrum (EIS) was collected in a frequency range from 100 k to 0.01 Hz at open circuit voltage.

1
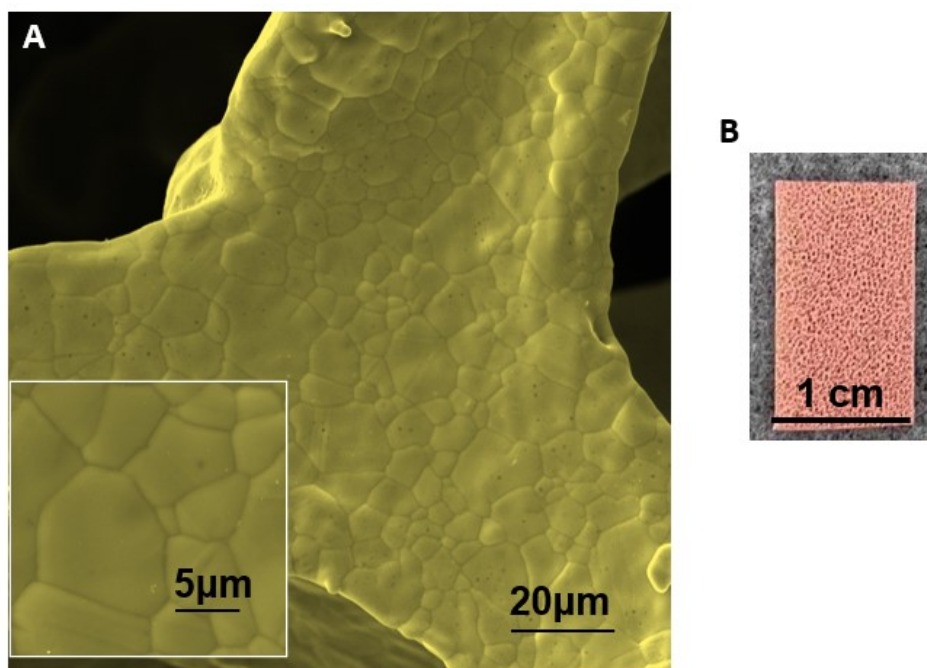
Figure S1. (A) Typical SEM image of Cu foam (CF), (B) Optical picture of CF.
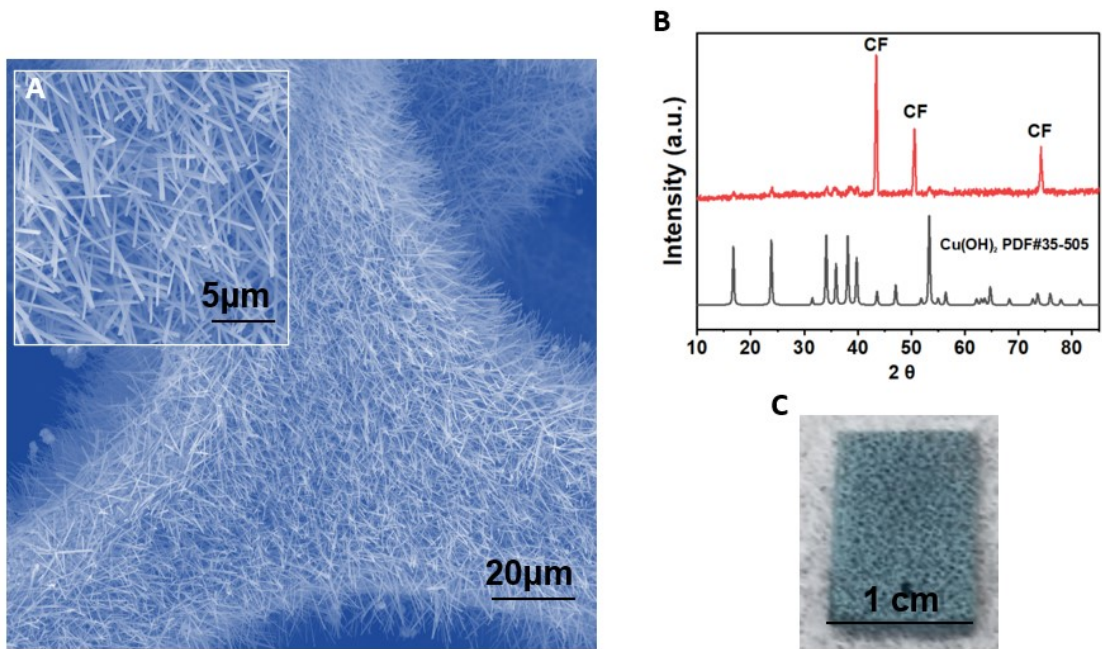
Figure S2. (A) SEM images, (B) XRD patterns of Cu(OH)$_2$ NWs and CF, (C) Optical picture of Cu(OH)$_2$ NWs.
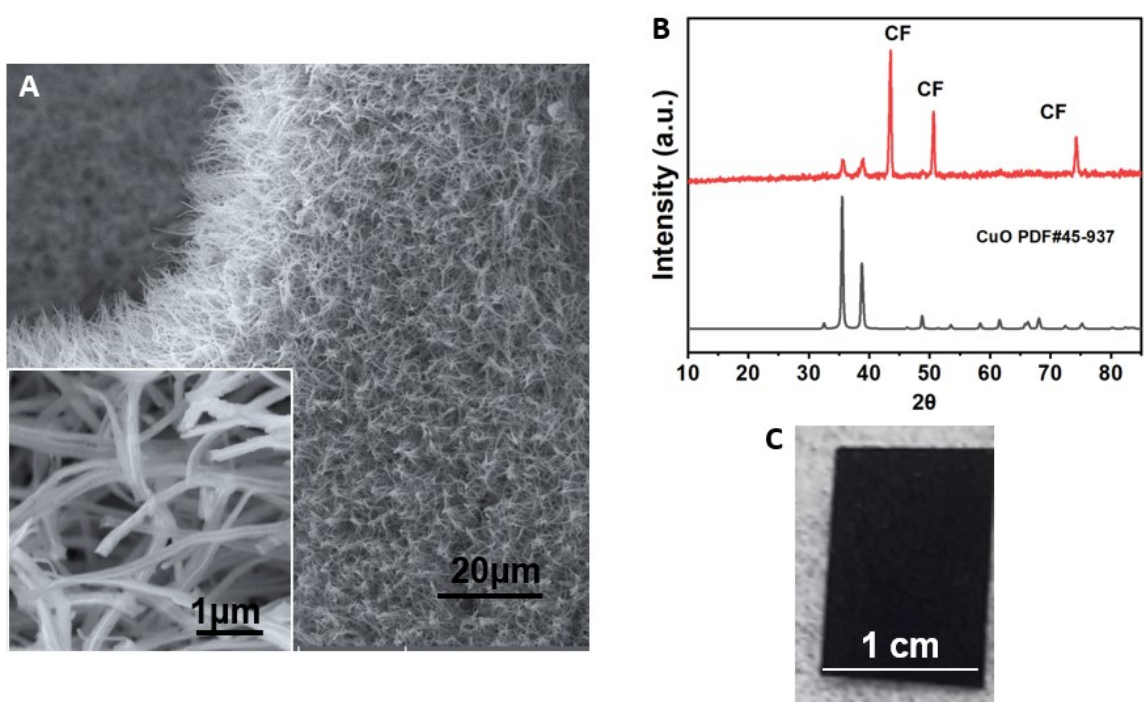
Figure S3. (A) SEM images, (B) XRD patterns of CuO NWs and CF, (C) Optical picture of CuO NWs.
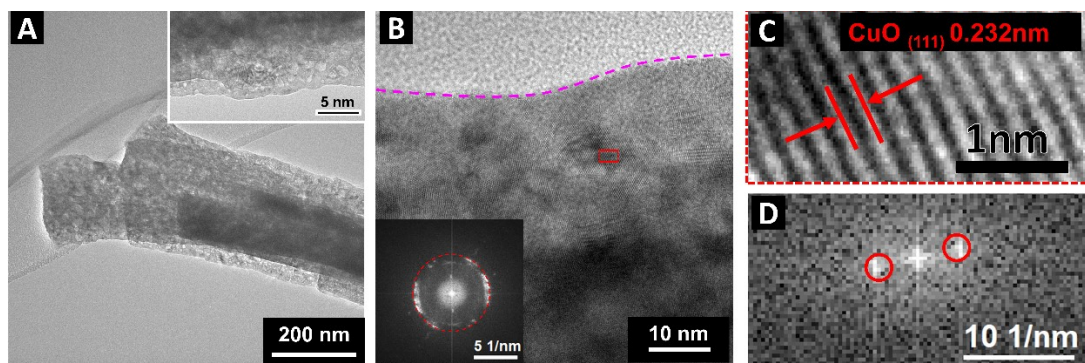
Figure S4. (A) Low-magnification TEM images of CuO NWs, (B, C) HRTEM images of the CuO NWs and corresponding fast Fourier transformation (FFT) image (D).
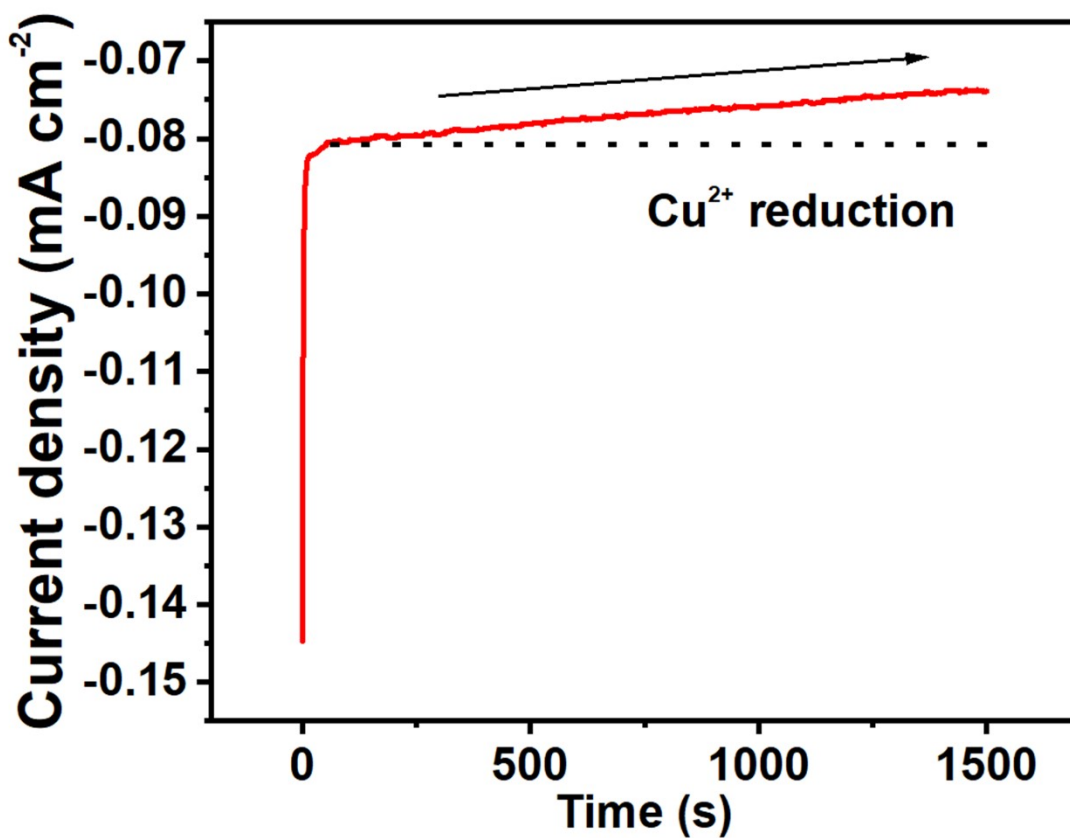
Figure S5. Electrochemical deposition i-t curve, the decreasing trend in current density means that the high price copper is reduced.
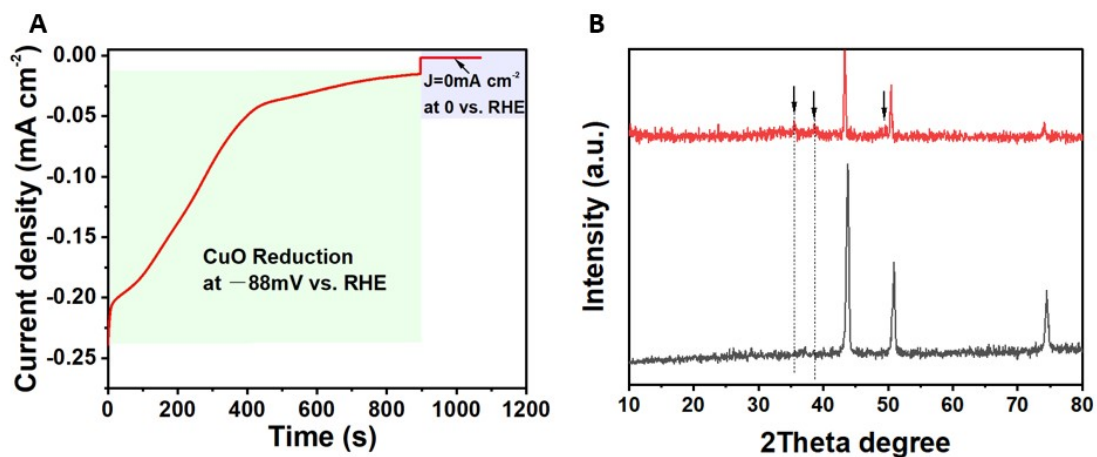
Figure S6. (A) The CH/LH@CuO$_x$ NWs with it-amperometric reduction (−0.1 V vs. RHE) for a certain time. The current density reaches to 0 mA cm^{-2} at 0V (vs. RHE) which means that all Cu^{2+} are reduced to Cu, (B) XRD patterns of CH/LH@CuO$_x$ NWs (red) and CH/LH@Cu NWs (black).
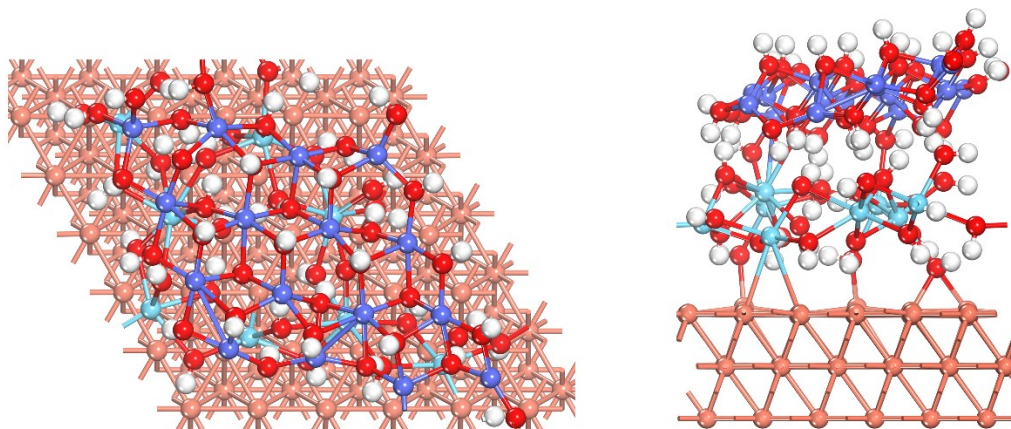
Figure S7. Schematic models of CH/LH heterostructure on Cu NWs.
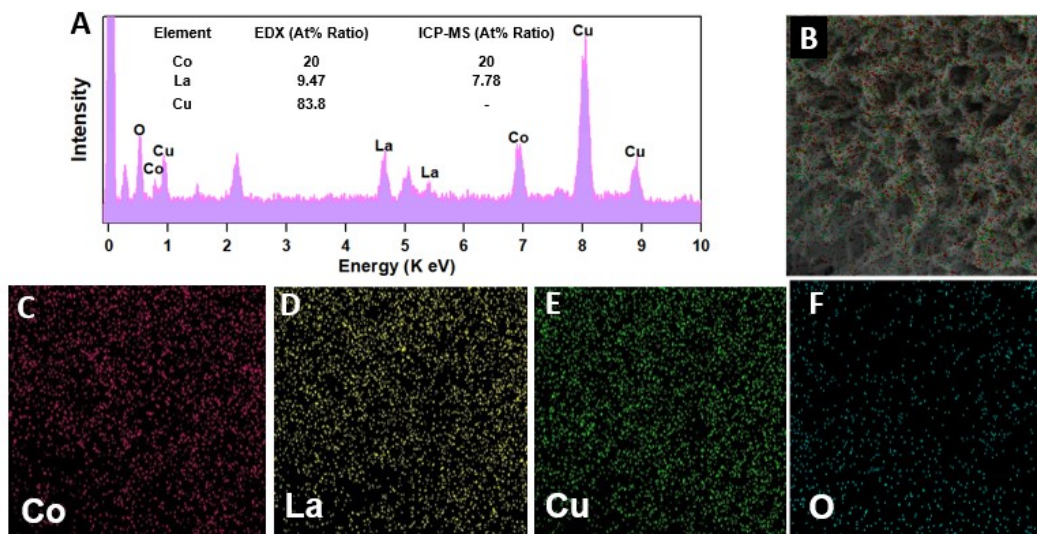
Figure S8. (A) EDX spectrum of CH/LH@Cu NWs (inset, At% ratio of EDX and ICP-MS) and (B-F) EDX mapping.
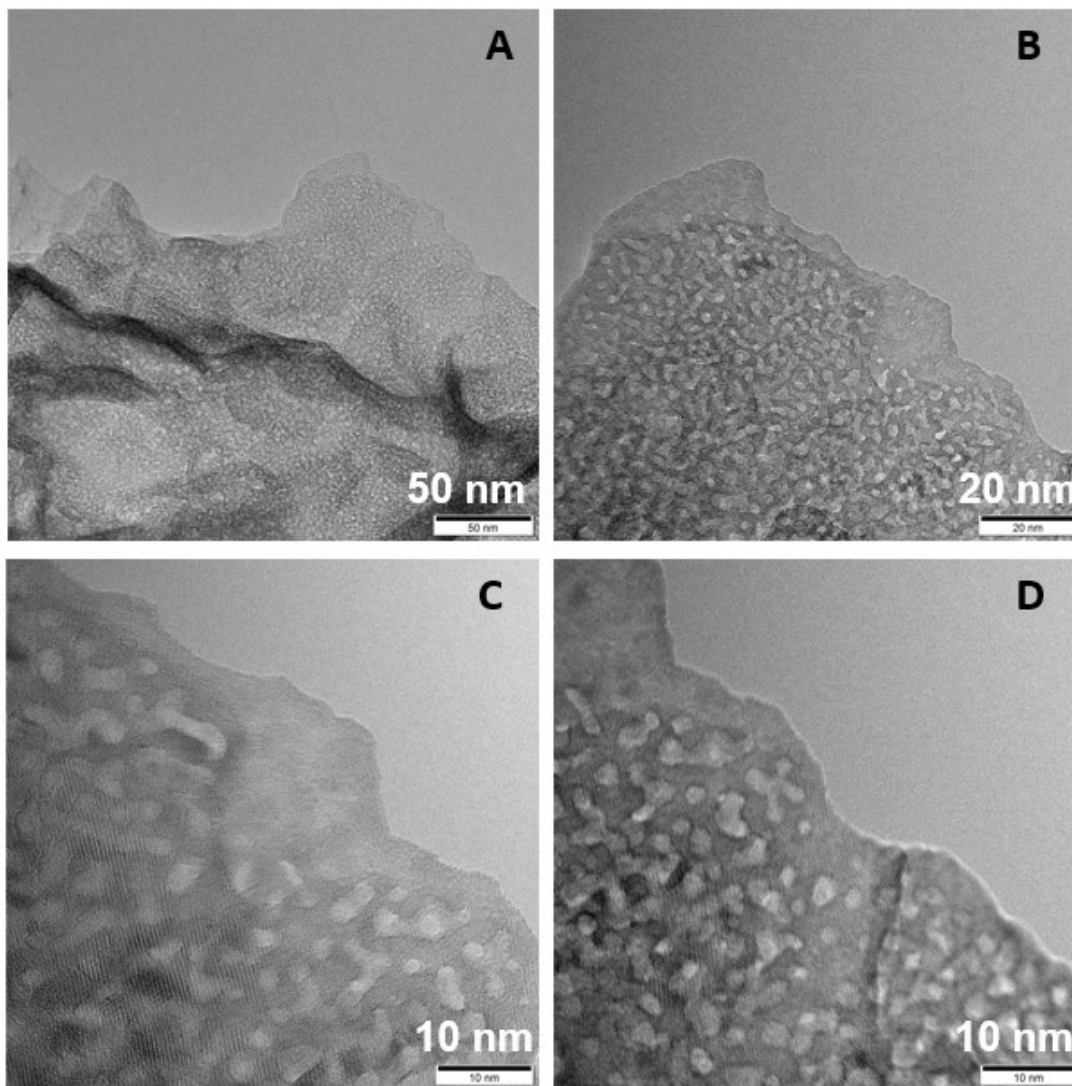
Figure S9. HRTEM image of the porous CH/LH@Cu NWs.
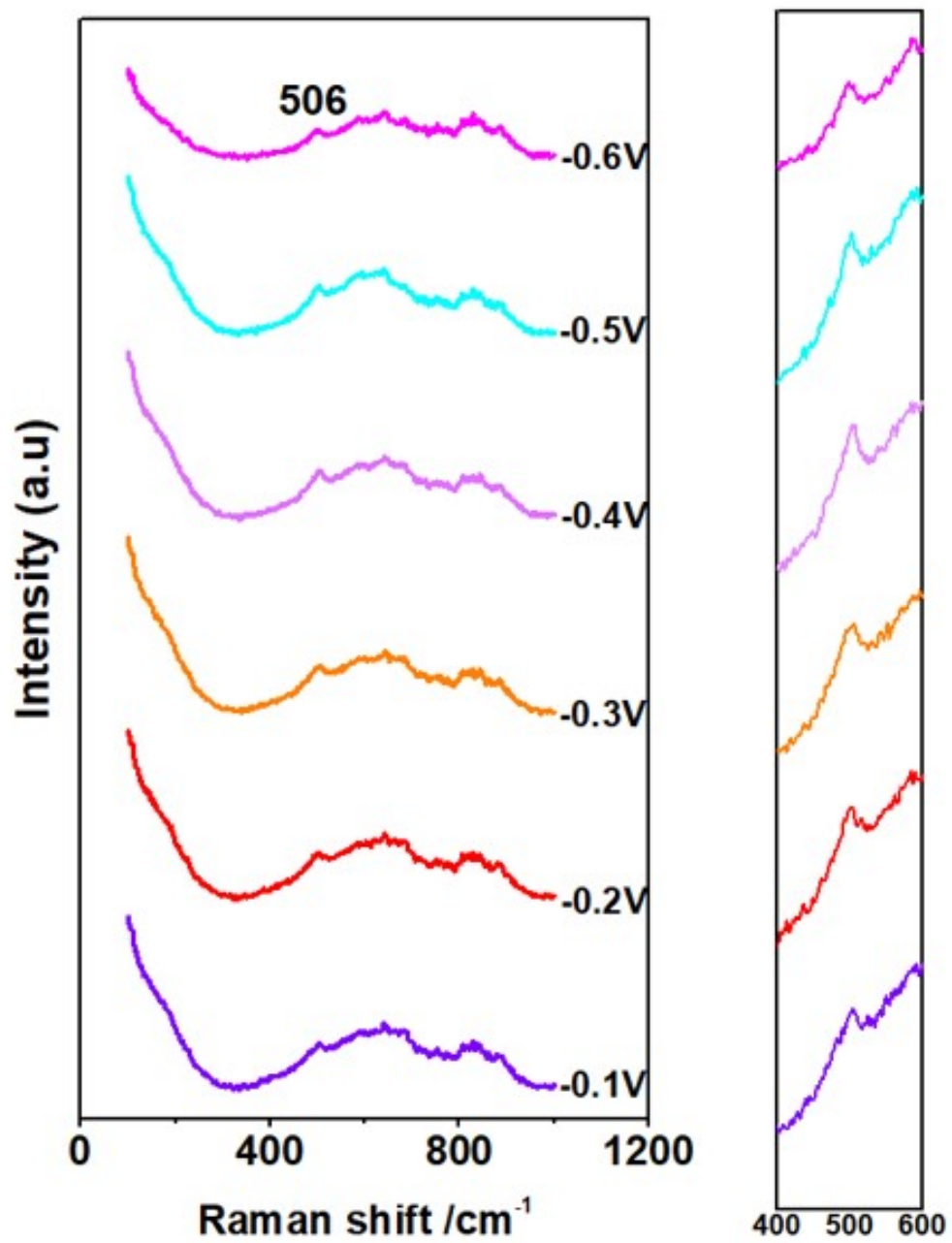
Figure S10. In situ Raman spectra of CH/LH@Cu NWs at a vary potential.
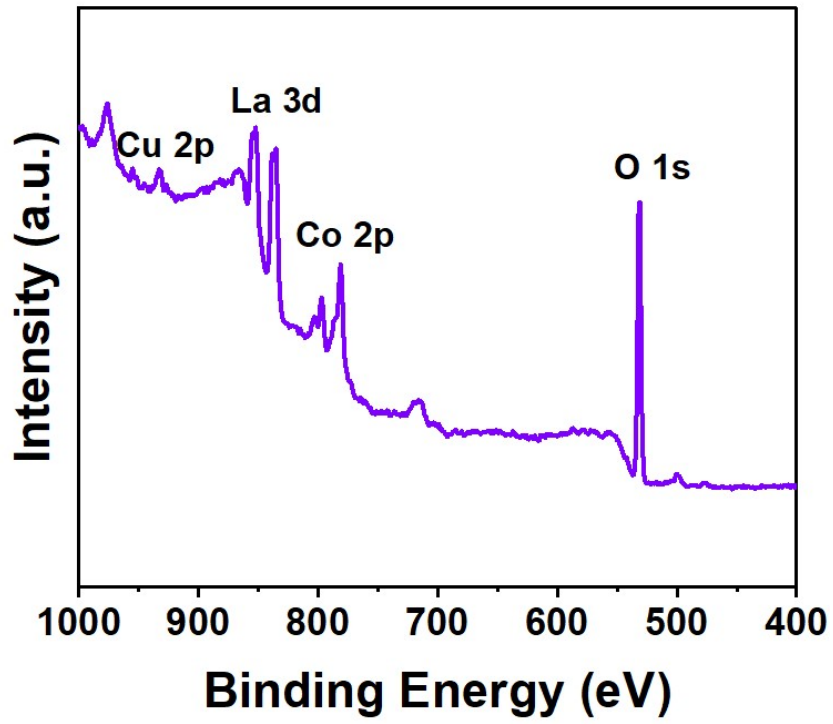
Figure S11. XPS survey of CH/LH@Cu NWs.
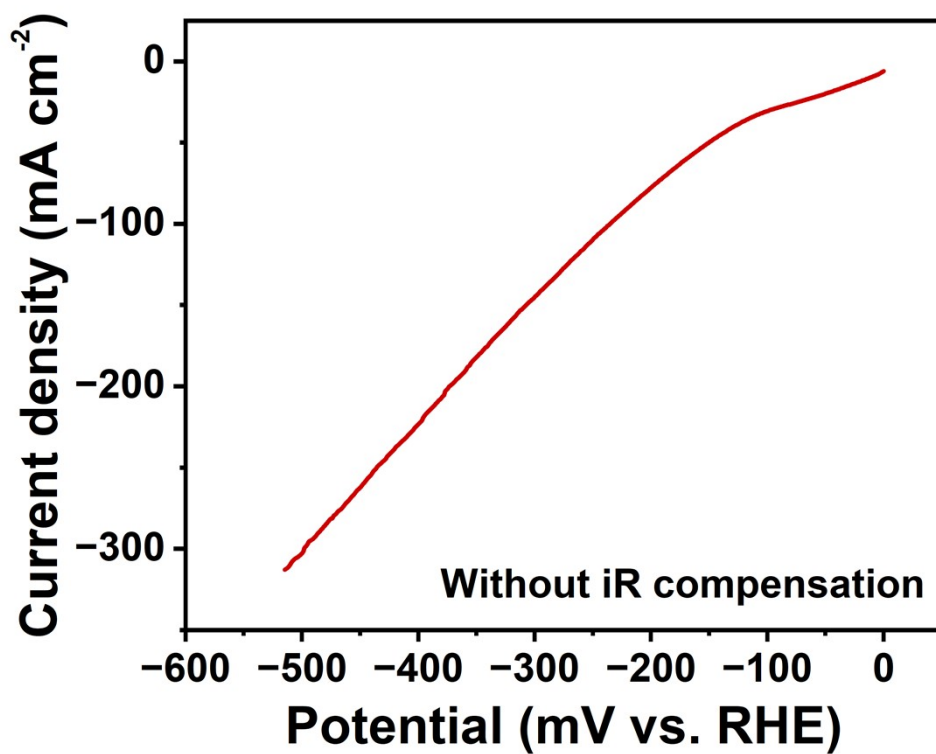
Figure S12. HER polarization curves of CH/LH@Cu NWs without iR correction.
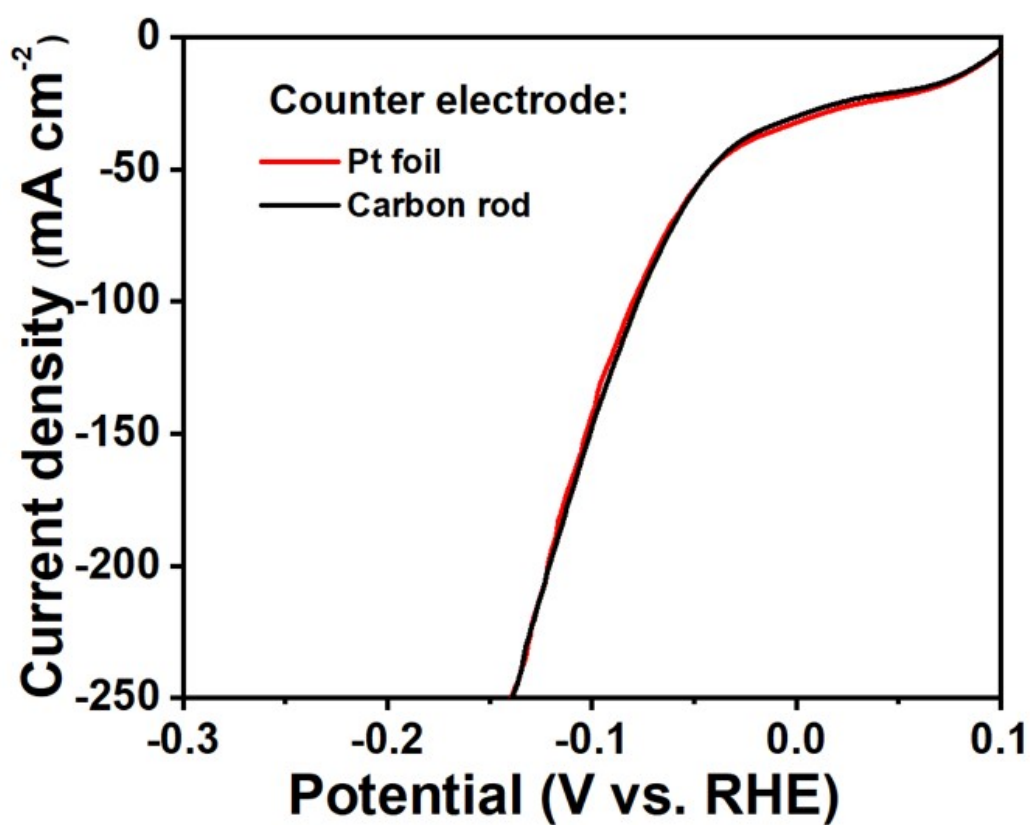
Figure S13. HER polarization curves of CH/LH@Cu NWs in 1 M KOH with graphite

rod and Pt foil as the counter electrode.
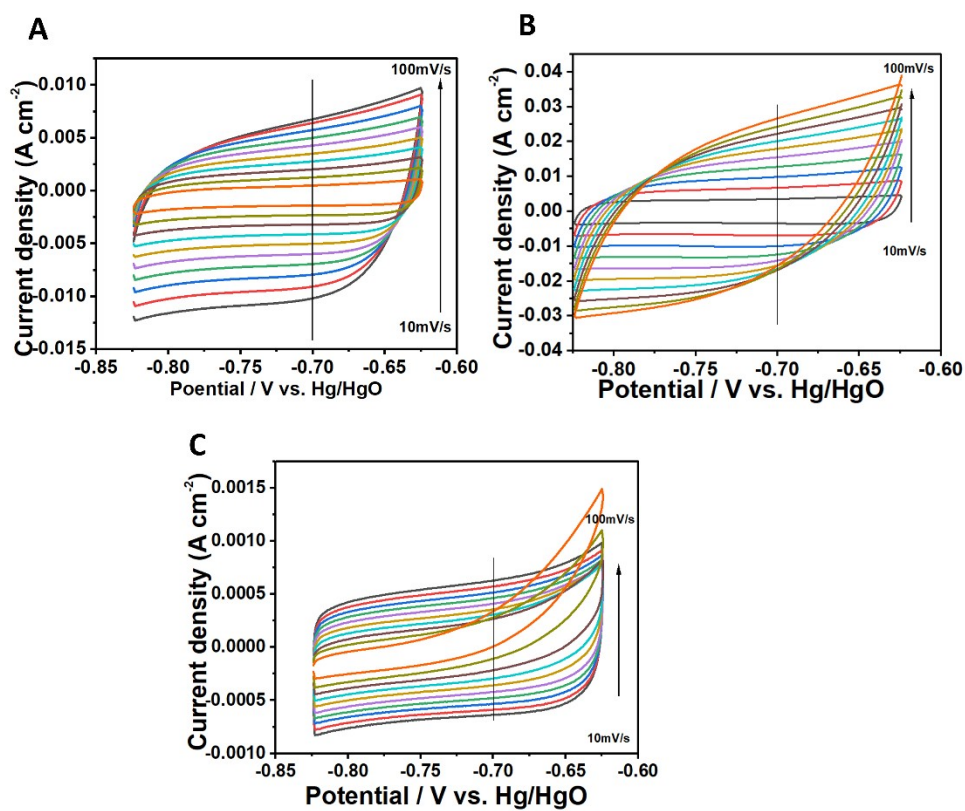
Figure S14. Scan rate dependence of the current densities in the CV curves of different HER catalysts with scan rates ranging from 10 mV s^{-1} to 100 mV s^{-1}. (A) CH/LH@Cu NWs, (B) Pt/C@Cu NWs, (C) CH/LH.
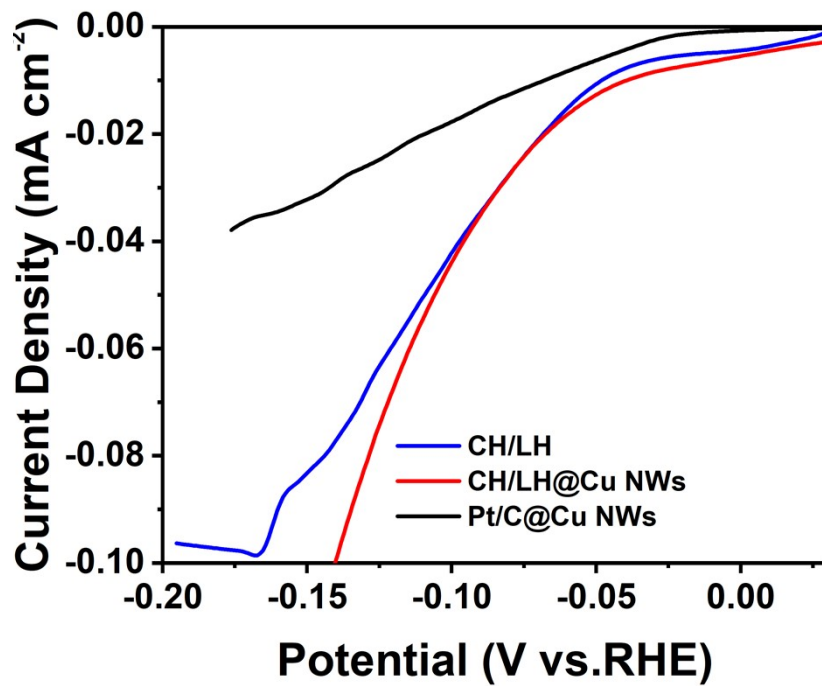
Figure S15. ECSA-normalized LSV curves of different catalysts for HER.
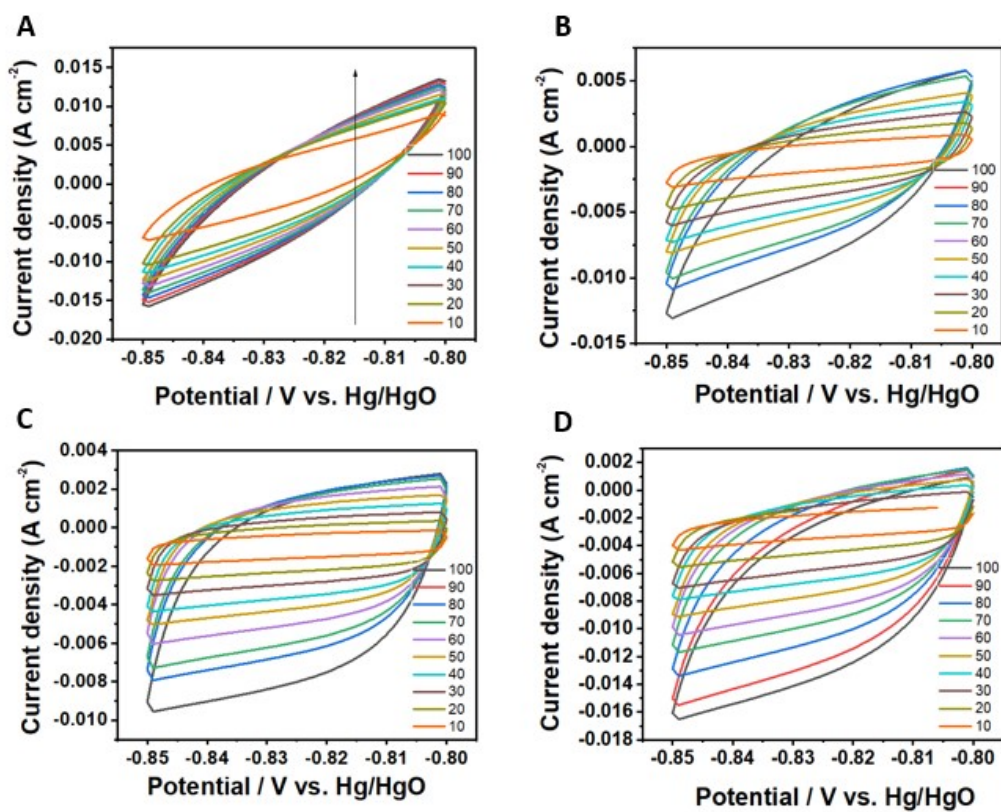
Figure S16. Scan rate dependence of the current densities in the CV curves of different HER catalysts with scan rates ranging from 10 mV s^{-1} to 100 mV s^{-1}. (A) Co(OH)$_2$@Cu NWs, (B) CH/LH@Cu NWs-1, (C) CH/LH@Cu NWs-2, (D) CH/LH@Cu NWs-3.

A

Co(OH)$_2$-001-3x3

Co(OH)$_2$-001-Hads2
$G_{H*} = 0.85$ eV

B

La(OH)$_3$-100-3x2

La(OH)$_3$-100-Hads2
$G_{H*} = 1.75$ eV
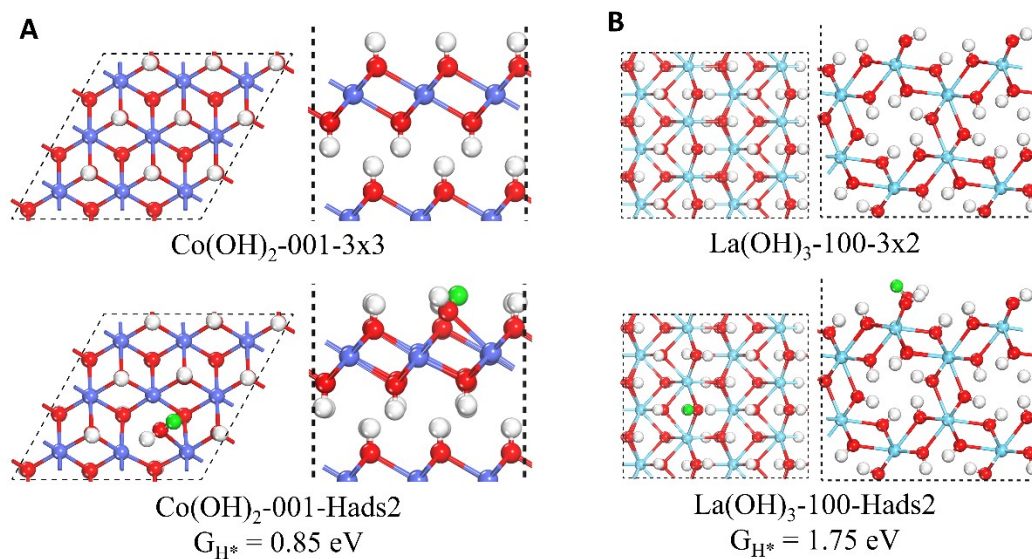
Figure S17. Schematic models of illustrate the (A) Co(OH)$_x$ and (B) La(OH)$_x$, as well as corresponding optimized structures of H* adsorption.
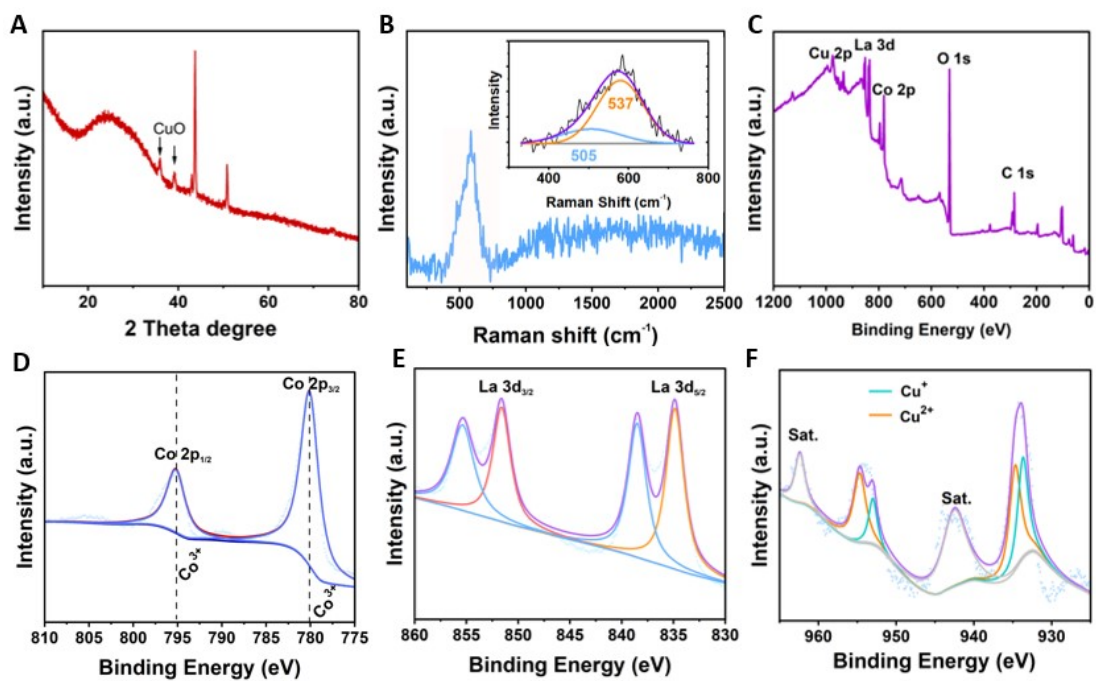
Figure S18. (A) XRD pattern, (B) Raman spectrum, (C) XPS survey and (D-F) high resolution XPS spectra of Co 2p, La 3d and Cu 2p for CH/LH@Cu NWs after OER.
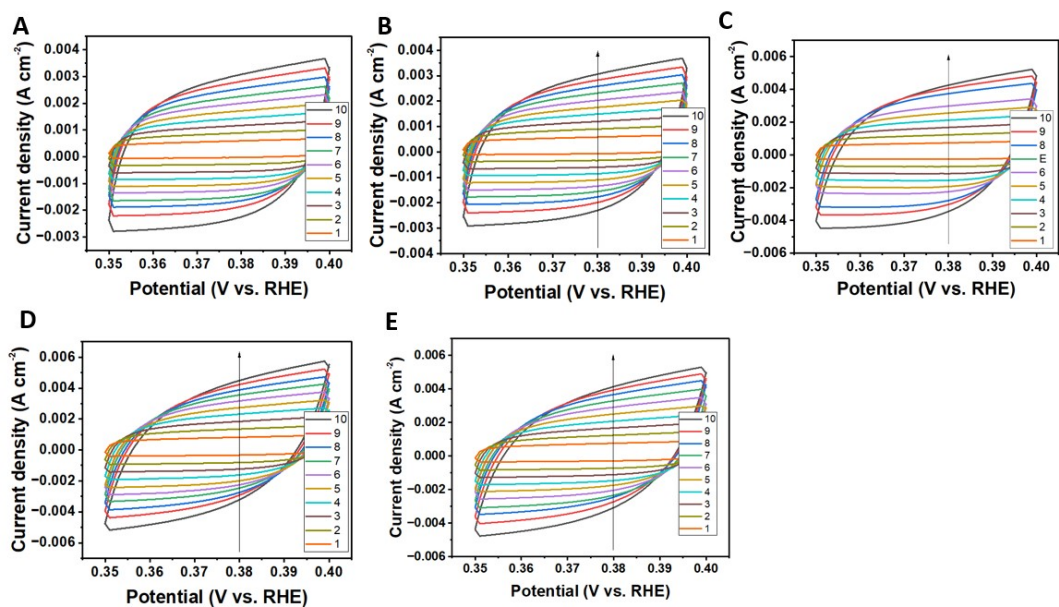
Figure S19. Scan rate dependence of the current densities in the CV curves of different OER catalysts with scan rates ranging from 10 mV s^{-1} to 100 mV s^{-1}. (A) La(OH)$_2$@Cu NWs, (B) La(OH)$_2$@Cu NWs, (C) CH/LH@Cu NWs-1, (D) CH/LH@Cu NWs-2, (E) CH/LH@Cu NWs-3.
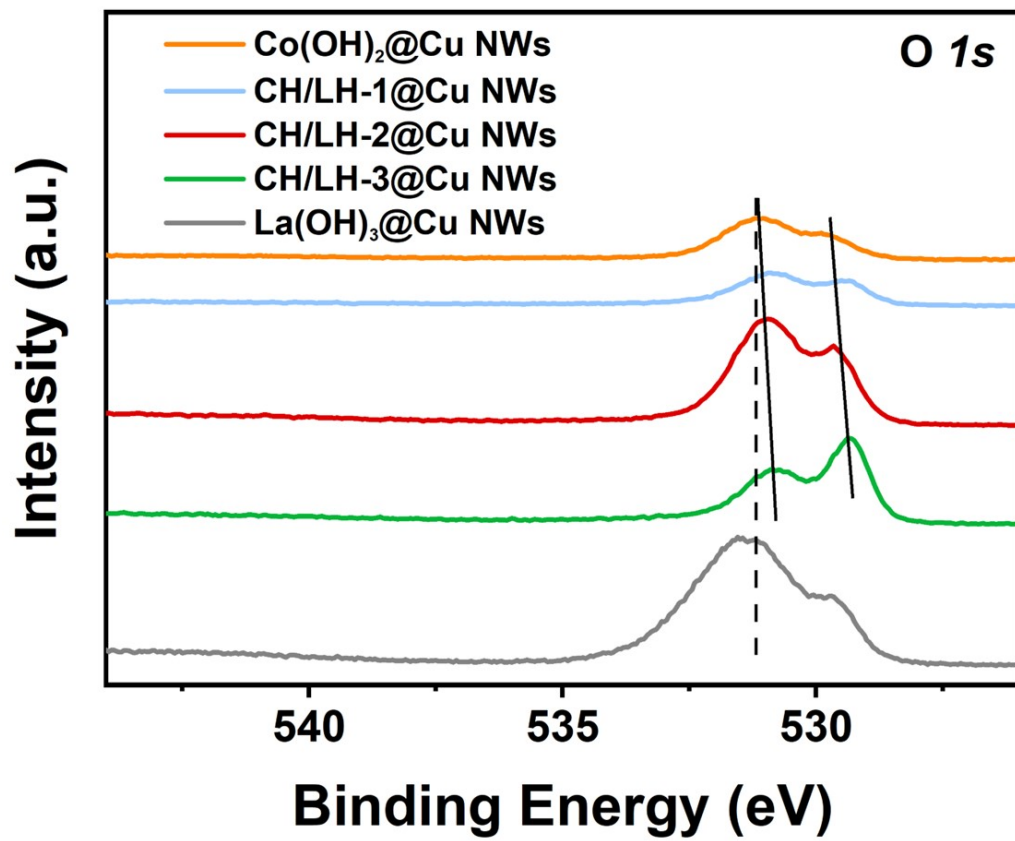
Figure S20. High resolution XPS spectra of O 1s for different samples.

A Co(OH)$_2$-001
G_{H*} = 1.57 eV

B La(OH)$_3$-100
G_{H*} = 2.22 eV

C CH/LH
G_{H*} = 1.47 eV

D
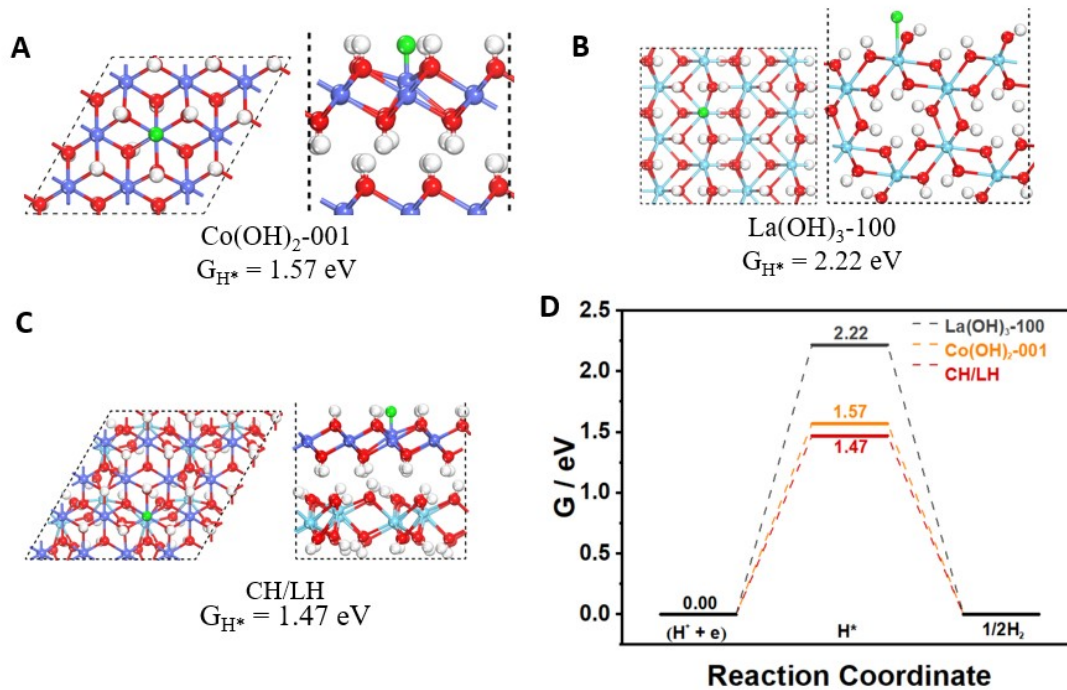
Figure S21. (A-C) Schematic models to illustrate the CH/LH@Cu NWs heterostructure and corresponding optimized structures of hydrogen specie adsorption at metal sites. (D) ΔG_{H*} simulated at the equilibrium potential for the La(OH)$_3$, Co(OH)$_2$ and CH/LH.
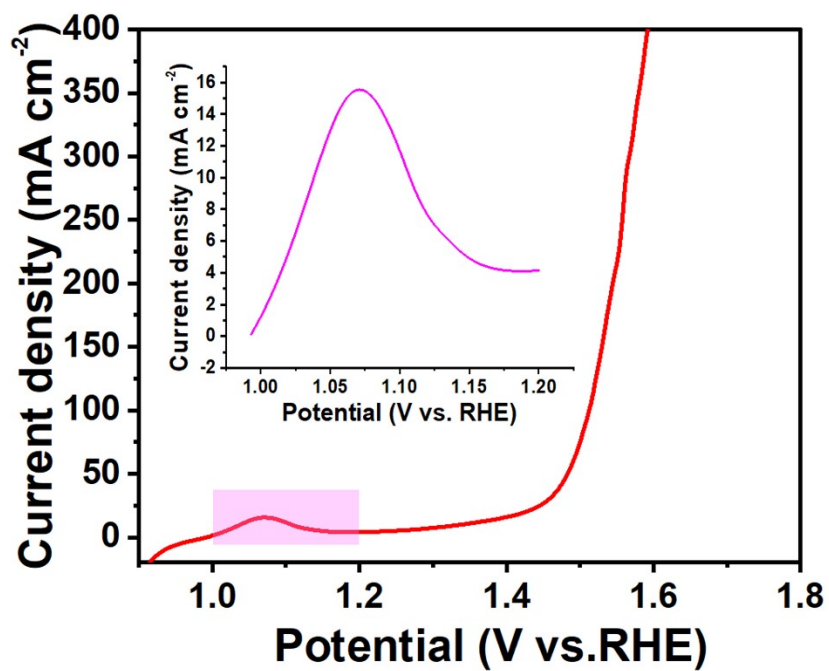
Figure S22. OER polarization curves of CH/LH@Cu NWs in 1 M KOH.
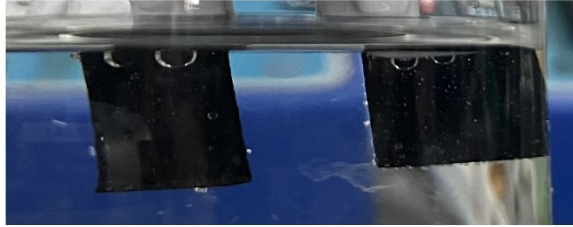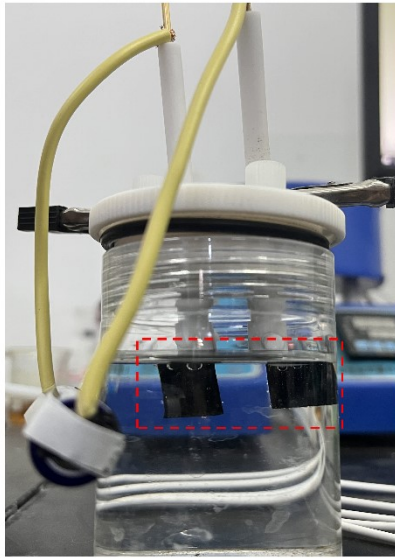
Figure S23. A single 1.5 V AA battery to drive the water splitting (CH/LH@Cu NWs || CH/LH@Cu NWs in 1 M KOH).

Table S1. The entropy and zero-point energy corrections in determining the free energy of hydrogen adsorbed on different catalysts.

Catalysts	$T \times \Delta S$ (eV) (298 K)	ΔE_{ZPE} (eV)
Co(OH)$_2$ (001)	0.02	0.28
La(OH)$_3$ (100)	0.01	0.28
CH/LH	0.02	0.03

Table S2. Comparison of the overpotentials demanded at 10 and 100 mA cm^{-2} as well as Tafel slope between our catalyst and recently reported HER catalysts (Unless otherwise noted, all of electrolyte are 1M KOH).

Electrocatalysts	HER@10 cm^{-2}	HER@100cm^{-2}	Tafel Slope（mV dec^{-1}）	Reference
CH/LH@Cu NWs	36 mV	75 mV	22.9	This Work
NiCoN|Ni$_x$P|NiCoN	165 mV	-	139.2	*ACS Energy Lett.* **2020**, 5, 2681[6]
MoO$_3$/Ni-NiO	152 mV	249 mV	36	*Adv. Mater.* **2020**, 32, 2003414[7]
P,S-Co$_x$O$_y$/Cu@CuS NWs	116 mV	-	139.2	*Adv. Funct. Mater.* 2021, 31, 2007822[8]
CuNi@NiFeCu	42 mV	-	133	*Appl. Catal., B* **2021**, 298, 120600[9]
Graphene/MoS$_2$/FeCoNiP$_x$	43 mV	127 mV	25.2	*Nat Commun* **2021**, 12, 1380 [10]
Co/CoMoN/NF	-	173 mV	68.9	*Adv. Sci.* **2022**, 9, 2105313[11]
Sn$_4$P$_3$	110 mV, 62 mV in 0.5 M H$_2$SO$_4$	-	139.2	*ACS Nano* **2022**, 16, 3, 4861[12]
CoFe-LDH@NiS	38 mV	238 mV	33	*Appl. Catal., B* **2022**, 308, 121221[13]

Table S3. Comparison of the overpotentials among our catalyst and recently reported OER and OWS catalysts (Unless otherwise noted, all of electrolyte are 1 M KOH)

Electrocatalysts	OER	OWS	Reference
CH/LH@Cu NWs	273 mV@100 cm^{-2}	1.56 V@20 cm^{-2}	This Work
Mo$_{51}$Ni$_{40}$Fe$_9$ NBs	292 mV@50 cm^{-2}	1.55 V@10 cm^{-2}	*ACS Catal.* **2019**, 9, 1013[14]
NiCoN|NixP|NiCoN	-	1.81 mV@10 cm^{-2}	*ACS Energy Lett.* **2020**, 5, 2681[6]
MoO$_3$/Ni-NiO	347 mV@100 cm^{-2}	1.55 mV@10 cm^{-2}	*Adv. Mater.* **2020**, 32, 2003414[7]
P,S-Co$_x$O$_y$/Cu@CuS NWs	280 mV@10 cm^{-2}	1.52 mV@10 cm^{-2} 1.77 mV@50 cm^{-2}	*Adv. Funct. Mater.* **2021**, 31, 2007822[8]
CuNi@NiFeCu	285 mV@50 cm^{-2}	1.51 mV@10 cm^{-2}	*Appl. Catal., B* **2021**, 298, 120600[9]
Graphene/MoS$_2$/FeCoNi(OH)$_x$	225 mV@500 cm^{-2}	1.59 mV@100 cm^{-2}	*Nat Commun* **2021**, 12, 1380 [10]
Co/CoMoN/NF	308 mV@100 cm^{-2}	1.56 mV@100 cm^{-2}	*Adv. Sci.* **2022**, 9, 2105313[11]
Sn$_4$P$_3$	169 mV@20 cm^{-2}	1.482 mV@10 cm^{-2}	*ACS Nano* **2022**, 16, 3, 4861[12]
CoFe-LDH@NiSe	127 mV@100 cm^{-2} 285 mV@100 cm^{-2}	1.51 mV@10 cm^{-2}	*Appl. Catal., B* **2022**, 308, 121221[13]

Reference

1.   G. Kresse and J. Furthmüller, *Physical Review B*, 1996, **54**, 11169-11186.

2.   P. E. Blöchl, *Phys Rev B Condens Matter*, 1994, **50**, 17953-17979.

3.   J. P. Perdew, K. Burke and M. Ernzerhof, *Phys Rev Lett*, 1996, **77**, 3865-3868.

4.   M. P. Teter, M. C. Payne and D. C. Allan, *Physical Review B*, 1989, **40**, 12255-12263.

5.   L. Gong, D. Zhang, C.-Y. Lin, Y. Zhu, Y. Shen, J. Zhang, X. Han, L. Zhang and Z. Xia, *Adv. Energy Mater.*, 2019, **9**, 1902625.

6.   L. Yu, L. B. Wu, S. W. Song, B. McElhenny, F. H. Zhang, S. Chen and Z. F. Ren, *ACS Energy Lett.*, 2020, **5**, 2681-2689.

7.   X. Li, Y. Wang, J. Wang, Y. Da, J. Zhang, L. Li, C. Zhong, Y. Deng, X. Han and W. Hu, *Adv. Mater.*, 2020, **32**, 2003414.

8.   T. L. L. Doan, D. T. Tran, D. C. Nguyen, D. Kim, N. H. Kim and J. H. Lee, *Adv. Funct. Mater.*, 2021, **31**.

9.   D. Cao, H. Xu and D. Cheng, *Appl. Catal., B*, 2021, **298**, 120600.

10.   X. X. Ji, Y. H. Lin, J. Zeng, Z. H. Ren, Z. J. Lin, Y. B. Mu, Y. J. Qiu and J. Yu, *Nat. Commun.*, 2021, **12**.

11.   H. Ma, Z. Chen, Z. Wang, C. V. Singh and Q. Jiang, *Adv. Sci.*, 2022, **9**, 2105313.

12.   S. Riyajuddin, M. Pahuja, P. K. Sachdeva, K. Azmi, S. Kumar, M. Afshan, F. Ali, J. Sultana, T. Maruyama, C. Bera and K. Ghosh, *ACS Nano*, 2022, **16**, 4861-4875.

13.   S. M. N. Jeghan, D. Kim, Y. Lee, M. Kim and G. Lee, *Appl. Catal., B*, 2022, **308**, 121221.

14.   X. L. Luo, Q. Shao, Y. C. Pi and X. Q. Huang, *ACS Catal.*, 2019, **9**, 1013-1018.